Invited Articles

Water entry of a flexible wedge: How flexural rigidity influences spray root and pressure wave propagation

Christine Gilbert,* John Gilbert, and M. Javad Javaherian†
Virginia Polytechnic Institute and State University, Blacksburg, Virginia 24061, USA

(Received 7 June 2023; accepted 18 August 2023; published 20 September 2023)

Wedge water entry can be used to study slamming on high-speed craft, seaplane landing, and biological flows such as birds diving into the water. The focus of this paper is on experimental measurements and simulations for the primary application of slamming of small craft, where the wedge boundary conditions are closed on all edges. The simulation is comprised of a one-way coupled nonlinear hydrodynamic code developed for water entry with an Euler-Bernoulli beam finite element solver. In this paper, the dynamic surface pressures on the bottom of the wedge are measured along with structural deflection, water contact line (or spray root), and rigid body motions of the vertically constrained wedge. Five different panel types with large variations in flexural rigidity were tested at impact speeds ranging from 1.2 m/s to 3.0 m/s. Comparisons of one set of experiments are compared with the simulation predictions. For the experimental results, it was found that the nondimensionalized spray root position versus time is self-similar despite the three orders of magnitude difference in the panel flexural rigidity values. When the time for the pressure wave to reach each pressure sensor on the bottom of the panel is normalized and compared with the hydroelasticity factor (the ratio of the structural period to the wetting time for the panel), the nondimensional times of arrival are approximately constant for each nondimensional location along the panel.

DOI: 10.1103/PhysRevFluids.8.090502

I. INTRODUCTION

Water entry research and experiments have numerous applications. Seemingly a fundamental problem in fluid-structure interactions, there is a rich amount of physics that can be explored. Water entry studies were first conducted for the application of seaplane landing in the 1930s [1,2]. Other aerospace applications of the water entry problem include water landing of spacecraft and solid water boosters as well as ditching of aircraft [3]. Applications in naval architecture include slamming of small craft in waves, wet-deck slamming of catamarans, and sloshing in a partially filled tank [4]. Additionally, there are bio-inspired flows such as birds diving in water [5] or the dynamics of human divers [6,7].

Slamming, shown in Fig. 1, occurs when high-speed planing craft operating in waves become airborne and reenter the water surface [8,9]. In rough water, these occur frequently and may injure passengers, compromise equipment onboard, damage the hull, and/or force operators to reduce their forward speed. An approximation can be used to reduce the study to that of a V-shaped wedge that vertically enters calm water since the cross-sections of most small, high-speed craft may be approximated by a V-shaped wedge. The wedge then represents a small section of the vessel that

*cmgilbert@vt.edu
†Present address: Naval Architecture and Marine Engineering, University of Michigan, Ann Arbor, MI 48109, USA.

(a) (b)

FIG. 1. Examples of small craft slamming. Courtesy of the Naval Surface Warfare Center Carderock, Little Creek Detachment.

vertically enters the water after becoming airborne, and it is possible to predict the hydrodynamics of these high-speed craft using the 2D+T theory or strip theory [9–11].

As a V-shaped wedge breaks through the undisturbed water surface, the resulting disturbance initiates water pile up and spray, as shown in Fig. 2. The spray root is defined as the point of maximum curvature on the water surface in close proximity to the body. There is a direct relationship between the instantaneous spray root position on the bottom of the wedge and peak pressure coefficient [12,13]. The nonuniform slamming pressure distribution for a single instant in time on the bottom of a V-shaped wedge is illustrated in Fig. 2. The peak pressure location and magnitude vary over time as they are functions of the submergence and the velocity of the body. After the spray root, a thin jet of water (spray) propagates away from the wedge [2,9].

The wedge water entry problem was first investigated for seaplane landings by von Karman [1], whose mathematical model presented a good macroscopic description of the problem. Wagner [2] developed the von Karman [1] model further by incorporating asymptotic theory. In this application, a V-shaped wedge was vertically driven into the water, so the formulation is similar for the vertical slamming condition. In the Wagner [2] formulation, the hydrodynamics and geometry are

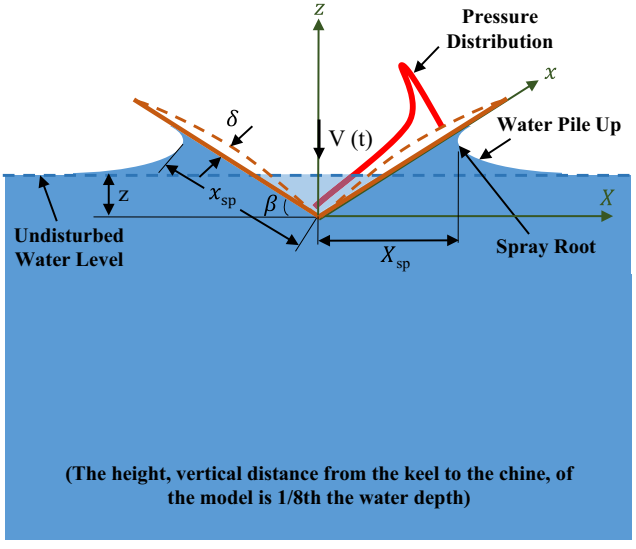

FIG. 2. Schematic showing the vertical wedge water entry physics at a time instant between the keel impact and chine impact moments.

considered to be linear. As a consequence, there exists a singularity at the spray root or wetted length, where the pressure goes to infinity.

To handle the singularity at the spray root present in the Wagner [2] model, researchers used an inner-outer solution technique [14–16]. The inner-outer solution entails solving two governing equations: one outside of the jet region (outer) and one inside the jet region (inner). To close the solution, a matching condition at the inner-outer domain boundary also must be applied [17]. Other researchers, such as Vorus [12], Judge *et al.* [13], Judge [18], and Xu [19], have expanded on the Wagner model by using the full nonlinear hydrodynamic terms in the governing differential equation. Retaining the nonlinear terms ensures that the singularity is eliminated without the use of an inner-outer solution scheme. This is computationally more expensive, but preserves the single solution field.

Experimentally, the rigid wedge problem has been studied by several researchers including Bisplinghoff and Doherty [20], Chuang [21], Judge *et al.* [13], Yettou *et al.* [22], Tveitnes *et al.* [23], Lewis *et al.* [24], and Ikeda and Judge [25,26]. The symmetric wedge with vertical drop was studied by Dobrovol'skaya [27], Zhao and Faltinsen [17], Korobkin and Scolan [28], Mousaviraad *et al.* [29] computationally. Pandey *et al.* [7] studied slamming forces across diving animals and humans in the laboratory using 3D printed rigid models. There have been numerous studies on the rigid wedge water entry problem; reviews of those works can be found in [3,30,31].

By relaxing the rigid assumption, the hydrodynamic slamming load can cause structural deformation to the wedge. When this deformation occurs, there is a change in shape/curvature of the plate panel, as shown by the dashed line on the wedge in Fig. 2. Due to the inward deformation of the panel, a pressure relaxation in the fluid can be observed in the near field [32]. In some cases, the full physics of the fluid-structure interaction problem needs to be assessed. Researchers such as Korobkin and Scolan [28], Faltinsen [30], Qin and Batra [33], Piro and Maki [34], Panciroli *et al.* [35], Panciroli [36], Panciroli and Porfiri [37], Mesa and Maki [38], Shams and Porfiri [39], Faltinsen [4], Ikeda and Taravella [40], Fisher *et al.* [41], Ren *et al.* [42] have examined this problem analytically and numerically for a deforming bottom panel on a V-shaped wedge. Additionally, experimental work has been conducted by Panciroli [36], Shams and Porfiri [39], Ren and Ikeda [43], Ren *et al.* [44–47], Javaherian *et al.* [48,49], Bhardwaj *et al.* [50], to name a few.

Faltinsen [30] proposed a nondimensional number to quantify the extent of hydroelasticity studying water entry of a wedge with a stiffened plate,

$$R = \frac{\tan\beta}{W_0}\sqrt{\frac{D_{22}}{\rho L^3}}, \tag{1}$$

where β, W_0, L, and D_{22} are deadrise angle, impact velocity, length of the wedge model, and flexural rigidity of the plate in the direction of bending, respectively. The hydroelasticity factor is a ratio between the total wetting time of the panel and the natural period of the panel. Large values of R mean that the structure is rigid, while low values of R indicate that the structural deformation influences the fluid pressure. A value of $R = 2$ was noted by previous researchers as a threshold value when considering maximum strain. Panciroli and Porfiri [37] used a similar expression for R, but replaced D_{22} with $Eh^3/12$ to go from a plate to a beam. Researchers, such as Piro and Maki [34], Shams and Porfiri [39], and Panciroli and Porfiri [37], started to use the hydroelasticity factor, R, and the critical value of 2 as proposed by Faltinsen [30]. The value of R does not have terms that account for the boundary conditions of the wedge and assumes fixed edges. This is a good approximation for the vehicle (aircraft, spacecraft, small craft) application.

In this paper, experiments and simulation predictions will be presented on the free-fall vertical water entry for a wedge with constant deadrise angle (20°) and five different panel types of varying flexural rigidity. The results from the simulation will be presented for one panel type for comparison. Experimental and numerical measurements include rigid body kinematics, pressure distributions and time histories, structural deformation of the bottom panel, and spray root time histories for the models. Section II of the paper provides a description of the experimental and numerical

TABLE I. Table of panels evaluated in this paper.

Panel name	Material	h (mm)	E_2 (GPa)	D_{22} (Pa m^3)	Schedule	Type of data
Rigid Aluminum	Alum 6061-T6	12.7	68.9	13 198	isotropic	Experiment
Composite Panel C	E-Glass/Epoxy	9.5	18.0	1631	90/90/45/ 0/0/0/0/0 −45/90/90	Experiment
Flexible Aluminum	Alum 6061-T6	3.17	68.9	205	isotropic	Experiment and Simulation
Composite Panel A	E-Glass/Epoxy	3.3	10.2	46.4	0/90/90/0	Experiment
Composite Panel B	E-Glass/Epoxy	3.55	7.49	40.0	0/0/0/0	Experiment

conditions. Following that section, the results for the experiments and simulations will be presented in Sec. III. Section IV provides in-depth discussion and further analysis of the results. The last section highlights the key conclusions from this work and future directions.

II. METHODOLOGY

The following two subsections outline the experimental program and the numerical program. Table I provides information on the five panels, which are studied in this paper. Each panel has a different flexural rigidity value, D_{22}, that was achieved by changing both the material stiffness and panel thickness, where

$$D_{22} = \frac{E_2 h^3}{12(1-\nu^2)}, \tag{2}$$

where E_2 is the stiffness of the panel in the direction of bending, h is the panel thickness, and ν is Poisson's ratio of the material. It is worthwhile to mention that the composite panels are made of E-Glass fiber with epoxy resin. The column designated as "Schedule" provides the orientation of the fibers relative to the keel of the wedge for each layer of fiberglass. All panels in Table I were evaluated in the experimental program and presented in this paper. In this paper, the comparison to the numerical simulations was only done for a flexible aluminum panel.

Table II shows the initial drop height of the conditions tested and their corresponding impact velocities. All conditions will be designated by their panel name and impact velocity. In the presentation of the results, the color gradient goes from dark to light as the impact velocity, W_0, increases.

TABLE II. The drop heights and corresponding impact velocities.

Drop Height (cm)	Approx. W_0 (m/s)
7.9	1.2
12.7	1.5
15.9	1.7
25.4	2.2
31.8	2.4
38.1	2.6
50.8	3.0

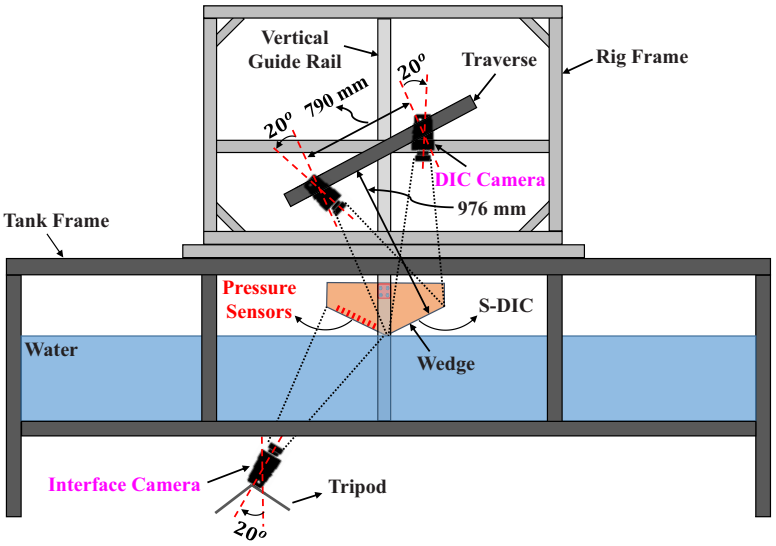

FIG. 3. Schematic of the experimental setup showing the wedge model above the water surface, the rig above the tank, the positions of the cameras above and below the tank, as well as the pressure sensor locations.

A. Experimental program

Figure 3 shows a schematic of the experimental setup. The experimental setup is a transparent water tank made of thick acrylic sheets supported by a steel frame. The overall dimensions of the tank are 4.4 m by 2.4 m and 1.2 m deep. The nominal water depth for these experiments is 0.83 m. The tank frame raises the tank off the ground by 0.7 m. Optical access below the tank allows for spray root measurements to be conducted. Above the tank is a rig built out of 80/20 T-slot aluminum. There are two vertical guide rails on which the wedge model slides from a designated drop height to the water surface. Linear bearings on each rail constrain the motion of the model in the vertical direction. There is a small amount of friction present in the system (observed to be no more than 4% by Javaherian *et al.* [49]). The current setup allows for drop heights up to 51 cm measured from the apex of the wedge to the calm water surface. To perform an experimental run, an electric crane is used to hoist the wedge to the desired drop height. The top of the wedge is attached to four electromagnets on the rig. When electrical power is turned off of the electromagnets, the wedge is released and the experiment is initiated. A pulse generator simultaneously deactivates power to the electromagnets and triggers all recording instrumentation. This provides synchronized measurements among all the instruments and cameras.

In this study, five wedge models with different bottom plate flexural rigidities are examined. For these wedges, side plates are 12.7 mm thick and are constructed from aluminum 6061-T6. The bottom panels are constructed from aluminum or fiberglass-epoxy as shown in Table I. The bottom plate thicknesses vary from 3 to 13 mm while the E_2 stiffness varies from 7 to 70 GPa. The panels were designed to have different D_{22} values to allow for variation in the hydroelasticity factor, R. To keep the overall mass the same for all the models, additional mass was added so that the total wedge mass was maintained at 40.6 kg.

Figure 4 shows a cross-section view of the wedge along with the mounted instruments. The vertical position time-history of the wedge apex during the impact event is recorded with an SGD-120-3 Resistive Linear Position String Potentiometer by Measurement Specialties. The string potentiometer is attached to the keel of the wedge so that the location of the keel during the experiments can be recorded (Fig. 4). This sensor has a measurement range up to 305 cm.

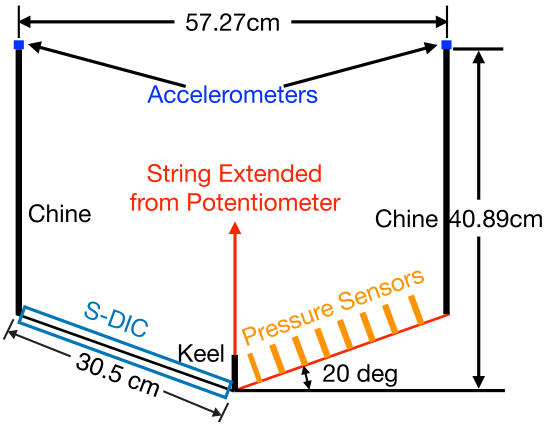

FIG. 4. Schematic of the wedge instrumented with accelerometers, string potentiometer, S-DIC side of the panel, and pressure sensor locations. The dimensions of the wedge are also provided.

Two miniature PCB-352A24 accelerometers, A_1 and A_2, are used to measure the vertical impact acceleration of the wedge. These accelerometers are located on top of the plate at both sides of the wedge (Fig. 4). The measurement range for these accelerometers is ± 50 g. The signal of these accelerometers are amplified by a PCB-482C05 signal conditioner. A DC response accelerometer PCB-3741B122G is also utilized to measure the low-frequency acceleration during the the free-fall. The measurement range of the DC accelerometer is ± 2 g. All AC and DC accelerometers record the acceleration with a sampling rate of 2 kHz.

Pressure measurements were taken using eight PCB-CA102B18 pressure transducers that are mounted on the bottom plate of the wedge (see Fig. 4). These sensors measure the dynamic pressure with a resolution of 0.007 kPa. A thermal ablative coating was applied on the diaphragm of the sensor to make it resistant against thermal shock in the measurement range of 344.7 kPa. The first sensor, P_1, is installed 33.9 mm away from the keel, and all other pressure sensors are located at increments of 33.9 mm along the centerline of the panel, as seen in Fig. 4. Two PCB-482C05 signal conditioners with four channels per unit are utilized to power, amplify, and condition the pressure sensors. The instantaneous impact pressure on the bottom of the wedge was captured at 200 kHz during the experiments. To ensure the flushness of the pressure sensors with the bottom plating, a sensitive LIDAR system is used. During the alignment process, the wedge bottom is illuminated with laser light, and the reflected light is analyzed by a transducer that records the distance between the wedge bottom and the transducer. The pressure sensors are then adjusted so that the diaphragm of each sensor precisely aligns with the wedge bottom plate with the order of 0.01 mm.

The Stereoscopic-Digital Image Correlation (S-DIC) technique is implemented to measure the structural response of the bottom of the wedge. This technique consists of two stationary high-speed Phantom VEO 710S cameras that are mounted on top of the rig on a traverse, which is located parallel to the bottom of the wedge at a distance of 976 mm (see Fig. 3). The location and angle of the cameras are set so that they can record overlapping images from the bottom plate of the moving wedge, which is coated by a high-density speckle pattern. These images are recorded at 2000 fps. Two powerful GSVITEC LED lights facilitate the recording by illuminating the measurement area. The S-DIC images are postprocessed using LaVision DaVis 8.0. The setup and calibration are optimized so that the displacement accuracy of 0.02 pixel is achieved.

During the wedge water entry, a spray root is formed on either side of the wedge bottom that propagates from the keel to the chine. A Phantom VEO 710S high-speed camera is located underneath the transparent tank (as shown in Fig. 3) to visualize the formation and evolution of the spray root on the bottom of the wedge during the impact. Similar to the S-DIC cameras, the spray root camera also records the event at 2000 fps with a resolution of 1280×800 pixels. The orientation

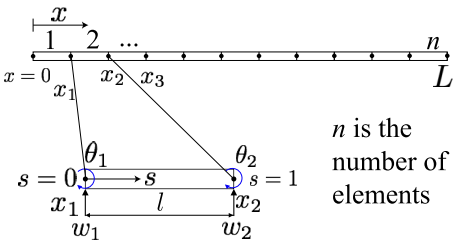

FIG. 5. Schematic of the 1D structural finite element model used to represent the behavior of the centerline of the wedge panel. The model is discretized using two-node beam elements with 2 degrees of freedom at each node.

of this camera is set so that it has a nearly perpendicular view to the bottom of the wedge. Images from this camera are synchronized with the data from other instruments with a delay of less than 100 ns. Uncertainties in the spray root measurement are outlined in more detail in [49].

B. Numerical program

The wedge water entry problem is typically characterized by fluid-structure interaction, nonlinear hydrodynamics, free-surface effects, and short timescales. For the numerical study, it is assumed inertial forces associated with the wedge motion are dominant over the time scales of interest ($\sim$100 ms) and viscous and gravitational forces can be safely neglected. Additionally, it is assumed that structural displacements are small enough to justify neglecting their impact on the adjacent flow field.

Under these assumptions, the water impact event is simulated in this study using a partitioned, one-way coupled fluid-structure solver. The fluid solver calculates the hydrodynamic loads, while the structural solver determines the dynamic response of the structure. The coupling between the solvers is such that changes in hydrodynamic loading affect the structure, causing it to deform, but changes in the structure do not influence the hydrodynamics. This one-way coupling allows for efficient and parallel computation of the fluid and structural domains, reducing computational costs compared to two-way coupled methods.

The hydrodynamic model assumes inviscid, incompressible flow, neglects gravity, and is based on the works of Vorus [12] and Xu [19]. Additionally, the specific hydrodynamic model used in this study incorporates subsequent refinements proposed by Judge [18]. The model combines geometric linearity with hydrodynamic nonlinearity to capture the significant flow perturbations resulting from water entry impact. To account for jetting effects, the spray root region is represented as a vortex distribution. This hydrodynamic model strikes a balance between computational feasibility and accuracy compared to the exact solution of the nonlinear ideal flow boundary-value problem and asymptotic theory [2,14,17].

For the structural domain, two key modeling simplifications are employed. First, the structural dynamics of the wedge are solved on a single side due to symmetry about the z-axis. Second, the modeling approach focuses solely on the midplane of the panel, where deflections are expected to be largest, and employs Euler-Bernoulli beam theory by assuming that three-dimensional effects along the midplane are negligible. A linear finite element solver is used to solve the structural domain. The structural model is constructed using two-node Euler-Bernoulli beam elements, with two degrees of freedom [deflection, $w(x,t)$, and rotation, $\theta(x,t)$] at each node, as illustrated in Fig. 5. Closed boundary conditions (Dirichlet) are applied at the keel [$w(x=0,t=0)=0$] and chine [$w(x=L,t=0)=0$] for all panels listed in Table I. Viscous stresses are neglected, and the only hydrodynamic load considered in the analysis is the dynamic pressure acting normal to the structure's surface. A Newmark-β scheme with $\beta = 1/4$ and $\gamma = 1/2$ is used to evolve the governing equations in time. While the Newmark scheme has some small amount of inherent

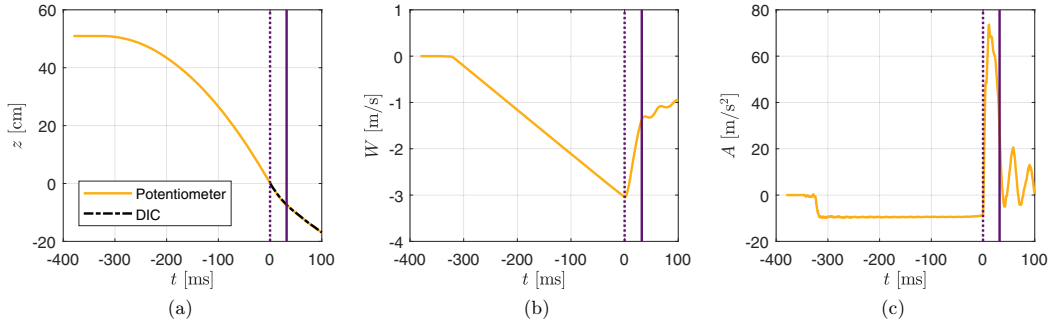

FIG. 6. Typical results for Composite Panel A at 3 m/s impact speed. (a) In the position, $z = 0$ corresponds to the calm water surface. The vertical lines indicate the time from the keel impact to the chine impact. (b) The vertical velocity was calculated by integrating the acceleration time history. (c) The experiment starts at the first dip in acceleration below 0 at about $t = -320$ ms. The free fall acceleration is seen until $t = 0$ when the keel impacts the water surface. Each curve represents an average of three repeated runs.

numerical dissipation, no additional structural damping is included in the model. The structural solver was verified and validated in [41].

III. RESULTS

A. Experimental results

The kinematic motions of composite panel A for an impact velocity of $W_0 = 3$ m/s are shown in Fig. 6. These figures show the full duration on the experimental run starting when the model is released from the electromagnets. In the case shown, the release of the model occurred at $t = -320$ ms. The dotted vertical line indicates the impact moment, which is the time when the keel touches the water surface. This was determined both by the string potentiometer and the high-speed camera located below the tank. The solid vertical line indicates when the chine wetted moment occurred. The time range between these two vertical lines is the time of interest in this experiment. In Fig. 6(a), the vertical position of the wedge recorded by the string potentiometer is also compared with that measured by the S-DIC cameras, which shows a very good agreement.

The vertical velocity, shown in Fig. 6(b), was not directly measured but was computed by taking the derivative of the position time history and the integral of the acceleration time history. The acceleration was measured using three accelerometers, and the resulting signal is shown in Fig. 6(c). The first accelerometer was a DC accelerometer and was only able to capture the time range from the start of the run until the impact moment ($t = 0$). The AC accelerometers are able to capture the dynamic acceleration peak and are placed on two sides of the wedge as a check for the symmetry of the drop. These signals are then averaged together to provide the acceleration signal from $t = 0$ and later.

Figure 7 shows a summary of all the conditions tested experimentally. The time ranges in these plots are consistent with the time range from the keel impact to the chine impact, where $t = 0$ is the time of the keel impact. The color gradient goes from dark to light as the impact velocity W_0 is increased. It is noted that uncertainties in the experimental measurements have been documented for three panels (rigid aluminum, flexible aluminum, and composite panel A) in [46].

The pressure time histories from each of the pressure sensors are shown in Fig. 8 for the rigid aluminum panel with $W_0 = 3$ m/s. The error bars represent the run-to-run variability over three repeated runs. For the rigid aluminum and flexible aluminum panels, one sensor was malfunctioning, so only seven sensors data are reported. The red vertical line at $t = 0$ marks the keel impact time, and the blue vertical line at $t = 30$ ms indicates the chine wetting time. The dip in pressure before the pressure peak is likely caused by the spray traveling over the pressure sensor before it becomes

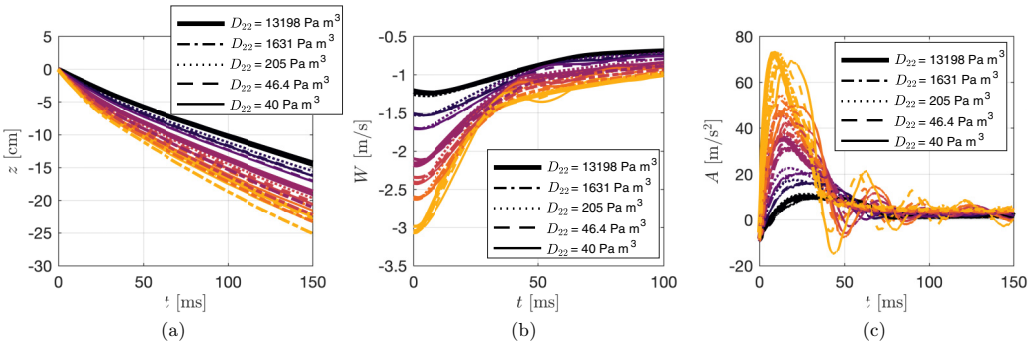

FIG. 7. Summary of all experimental conditions for (a) keel submergence, (b) keel velocity, and (c) vertical acceleration results for all conditions from keel impact to chine wetting time. Each curve represents an average of three repeated runs. The color scale goes from dark to light with increasing impact velocity, W_0, that is tabulated in Table II.

submerged in the water [46]. The peak in the signal indicates when the peak pressure reaches the location of each sensor, and further analysis on this will be discussed in Sec. IV.

Figure 9(a) shows a single frame from the high-speed camera video of the spray root movie. The red line denotes the spray root. This line was calibrated as the spray root line as discussed in [49]. Javaherian *et al.* [49] recorded high-speed movies of the spray root from the side and bottom of the wedge at 2000 frames per second. They used gradient-based edge detection to determine the shape of the curve due to changes in gray scale level. They found that the spray root identified in the bottom camera was within $\pm 1.5\%$ of the spray root identified in the side view camera. The spray root for different time steps is then extracted and plotted in Fig. 9(b). Since the pressures are measured at the centerline of the wedge, the spray root was identified at the centerline of the wedge, shown as the red dashed line in Fig. 9(b), and reported in Fig. 10 for $D_{22} = 46.4$ Pa m^3 with impact velocity W_0 specified in the legend. These results are representative of results seen in other panels.

Measurements from the S-DIC method were taken as displacements. The vertical displacement was taken at the midspan of the wedge. Further details of past measurements are documented in [46,49]. One deflection curve (from the midspan) was taken at discrete time steps during the

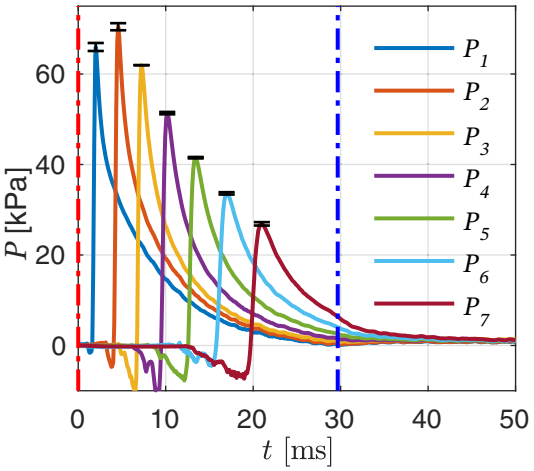

FIG. 8. Pressure signals from seven sensors for a rigid aluminum panel with an impact speed of $W_0 = 3$ m/s.

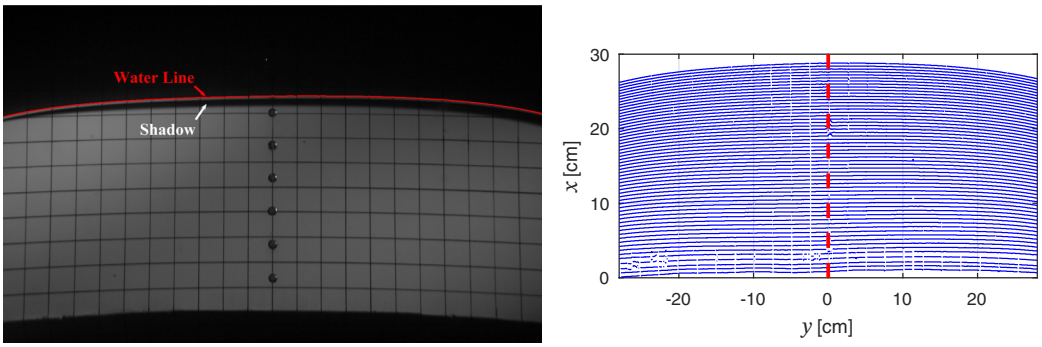

(a) (b)

FIG. 9. (a) Single frame from the bottom view camera. The red line denotes the spray root [49]. (b) The results from the spray root taken from the high-speed videos. The red dashed line indicates the location, at the centerline of the wedge, that the spray root position time histories are reported in Fig. 10.

experiment. The maximum deflection value on the curve was plotted versus time for each panel condition and impact velocity condition in Fig. 11.

B. Numerical results

The numerical model described in Sec. II B was used to simulate water entry of the flexible aluminum panel. The simulation start time ($t = 0$) coincides with the time when the keel initially impacts the calm water surface, and it terminates when the spray root reaches the chine (i.e., a "chine wetted" condition). For the flexible aluminum panel, this occurs between 35 and 70 ms, depending on the impact velocity. In each of the simulations, the finite element beam model was discretized with 64 elements, and the coupled simulation was evolved in time using a constant time step size of $\Delta t = 0.1$ ms.

Figure 12 provides a comparison between the numerical predictions of wedge kinematics and experimental observations. Acceleration time histories predicted by the simulation show minor differences with the experiment for the low impact speeds at early times, but the higher impact

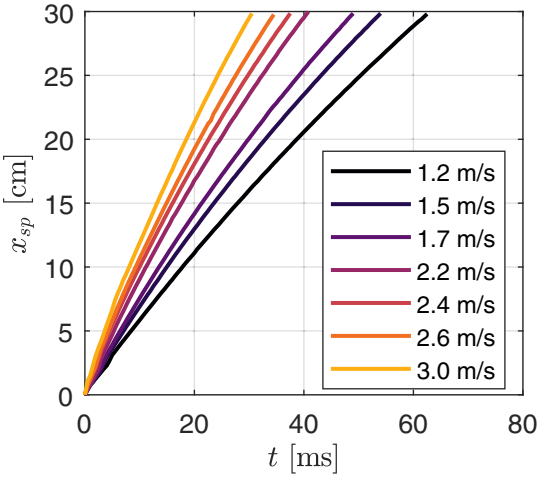

FIG. 10. Spray root position time history from the bottom view camera with the spray root location taken at the midspan of the panel for $D_{22} = 46.4$ Pa m^3 (composite panel A) with impact speed indicated in the legend.

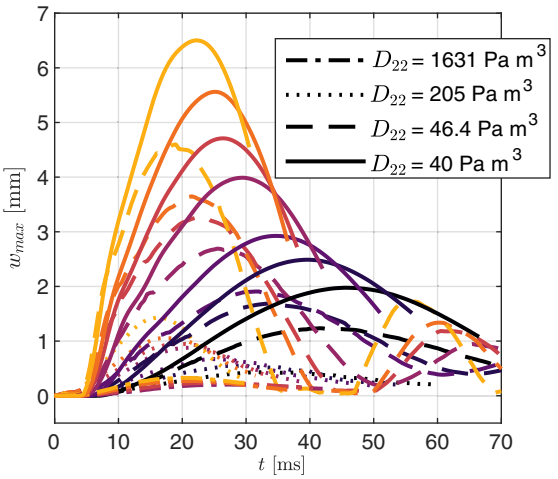

FIG. 11. Maximum deflection time history for all experimental results. Different line styles correspond to the different panels, and the color gradient becomes lighter as the impact velocity increases.

speeds show good agreement. Peak acceleration is captured well across all impact velocities. Model predictions of keel position and velocity agree well with experiments and are less sensitive to the early-time discrepancies in wedge acceleration seen at low drop heights.

Figure 13 shows model predictions of hydrodynamic pressure and the corresponding structural deflection along the beam compared with experimental observations. The distributions shown correspond to the times when the peak of the pressure wave reaches each sensor location. Predictions for time of arrival of the pressure wave at each sensor location are all within 1 ms of the experiment. The hydrodynamic model accurately captures the peak pressure early in the simulation ($t < 10$ ms), but underpredicts the peaks as the pressure wave moves beyond the third sensor position. The deflection distributions predicted by the numerical model are qualitatively similar to experimental S-DIC measurements, but they tend to overpredict the amount of deformation experienced by the wedge panels at high impact velocities and underpredict the deformation at low impact velocities.

The same trend is observed in Fig. 14, which shows deflection distributions resulting from the Euler-Bernoulli beam model compared with the S-DIC measurements. Results correspond to the time at which the overall maximum deflection occurs for each drop condition. At the higher impact velocities, the actual panel geometry and boundary conditions (fixed edges along the front

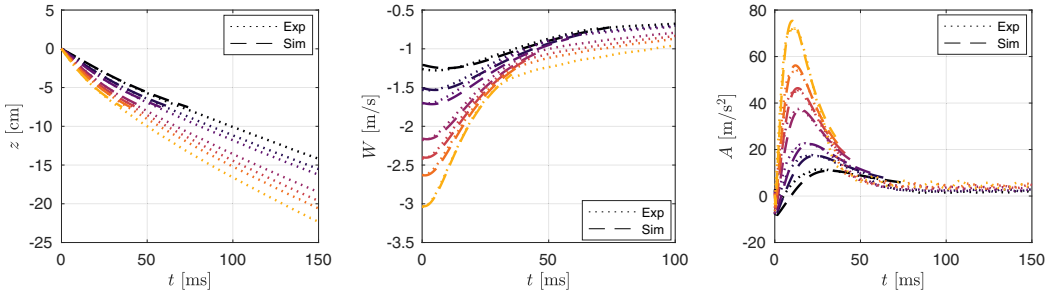

FIG. 12. Summary of kinematics for all flexible aluminum numerical and experimental results. (a) Keel submergence, (b) keel velocity, and (c) vertical acceleration from keel impact to chine wetting time. The color scale goes from dark to light with increasing impact velocity, W_0, which is tabulated in Table II.

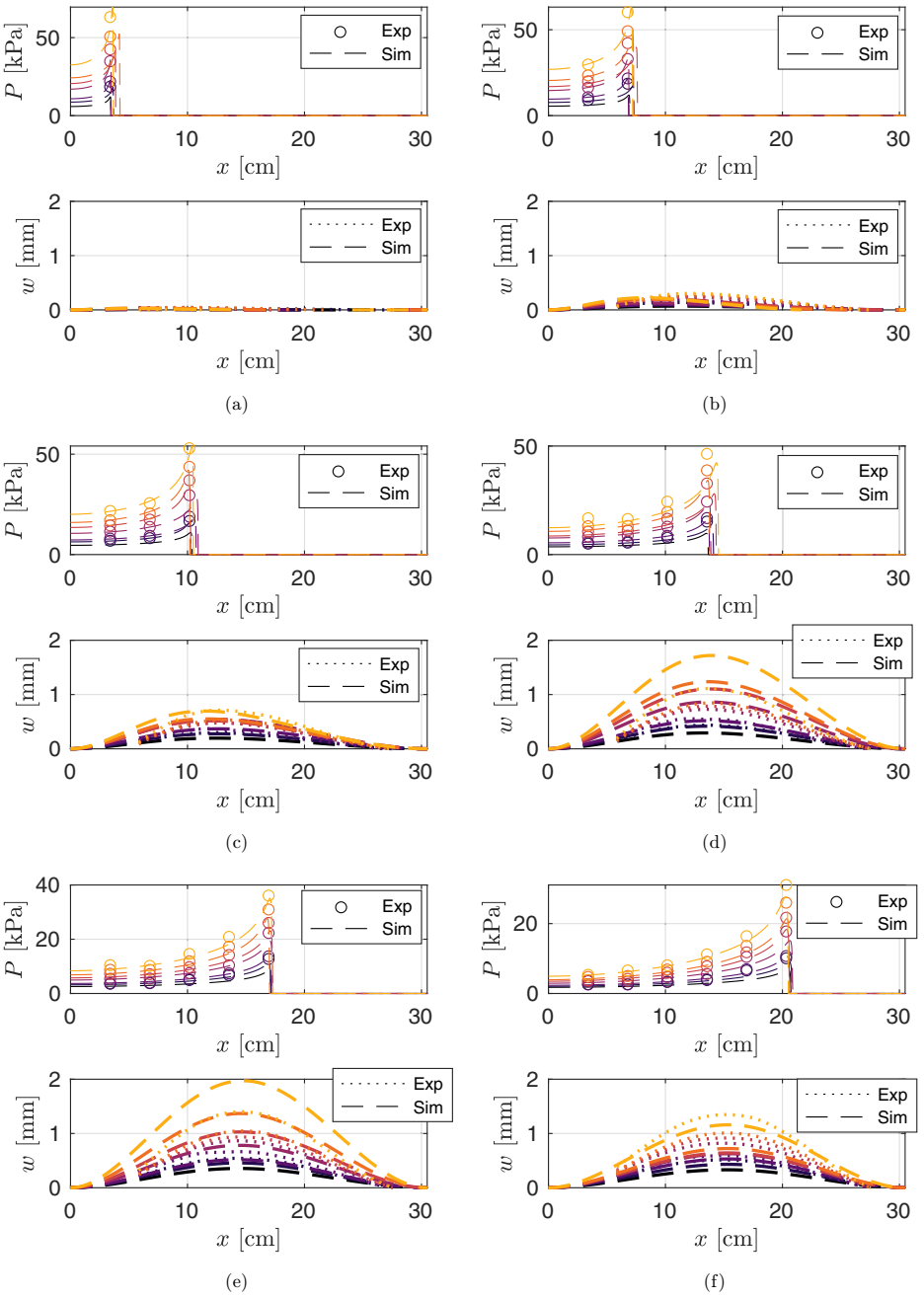

FIG. 13. Model predictions of hydrodynamic pressure and structural deformation compared with experimental pressure sensor and S-DIC measurements. (a)–(f) Distributions shown correspond to the time of arrival of the peak of the pressure wave at sensors P1–P6. The color gradient becomes lighter as the impact velocity increases.

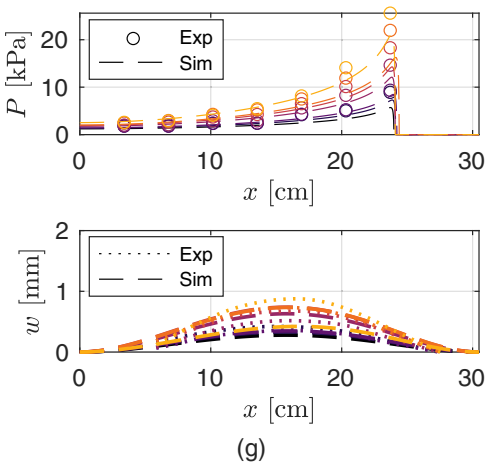

FIG. 13. (*Continued*). Model predictions of hydrodynamic pressure and structural deformation compared with experimental pressure sensor and S-DIC measurements. (g) Distributions shown correspond to the time of arrival of the peak of the pressure wave at sensor P7. The color gradient becomes lighter as the impact velocity increases.

and back of the model) play a larger role in the panel dynamics which the Euler-Bernoulli beam approximation is unable to accurately capture. The lower deflections predicted by the model at the low impact velocities are a result of the hydrodynamic model underpredicting the dynamic pressure along the panel surface. Figure 15 shows the maximum deflection predicted by the simulation as a function of time, which results from recording the maximum deflection along the length of the beam at each simulation time step. Results from the lower impact velocities are qualitatively similar to those seen in the experiment. At higher impact velocities, the structural model predicts vibrations not seen in the flexible aluminum S-DIC data; however, these oscillations were observed experimentally in the responses of the composite panels which experience larger deformations than the flexible aluminum panel. This may be due to the absence of structural damping in the numerical model.

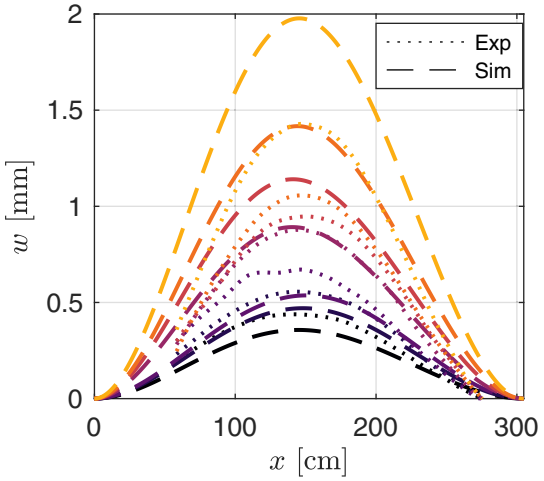

FIG. 14. Deflection distribution at the time when the maximum deflection occurs for the flexible aluminum experiments and simulations. The color gradient becomes lighter as the impact velocity increases.

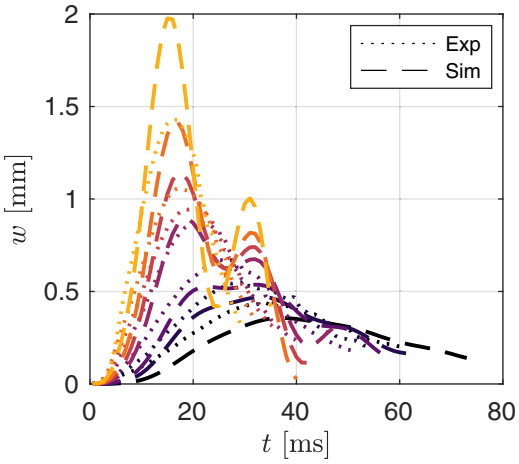

FIG. 15. Maximum deflection time history for flexible aluminum experiments and simulations. The color gradient becomes lighter as the impact velocity increases.

IV. DISCUSSION OF RESULTS

The spray root time histories are shown for all panels and all impact velocities in Fig. 16 for the experimental program. The color gradient from dark to light color corresponds to increasing impact velocity, W_0. For lower impact velocities, and darker colored lines, there is clustering for different D_{22} values in the results. As the impact velocity increases, the spray root curves spread out more with the highest D_{22} panel having the highest velocity or slope of the curve. This makes sense as the impact velocity corresponds well with the spray root velocity. Furthermore, the higher the D_{22} of the panel, the more rigid the panel is. This means it will deform less. As the panel curves inward due to the inward hydrodynamic pressure, the distance that the spray root and pressure wave must travel increases slightly. This means that the spray root will appear slower when there is more deformation of the panel. For a deeper discussion on the relationship between the spray root dynamics and panel rigidity, the interested reader is referred to Javaherian *et al.* [48].

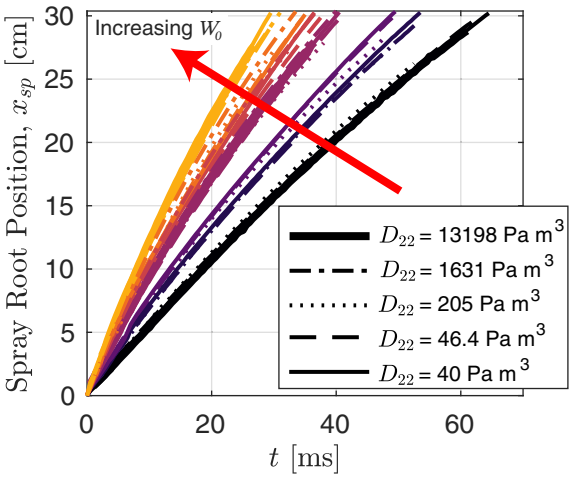

FIG. 16. Summary of spray root position time histories for all panels in the experimental program at all impact velocities. The color gradient becomes lighter as the impact velocity increases.

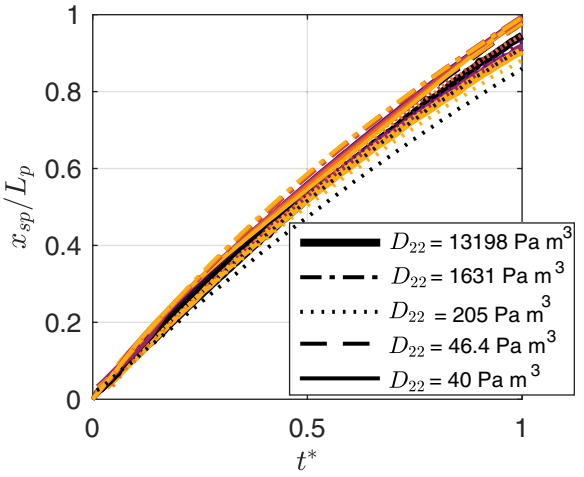

FIG. 17. Summary of nondimensional spray root time histories in the experimental program. Position is normalized by the length of plate the spray root must travel, and the time is normalized by the wetting time. The color gradient becomes lighter as the impact velocity increases.

To make more sense of this, the spray root time history plot was nondimensionalized in Fig. 17. The spray root position was normalized by the panel length (the length along the incline from the keel to the chine, which is constant for all conditions and 30.5 cm in length) and the time was normalized by the wetting time, the time it takes for the spray root to travel from the keel to the chine. The resulting plot shows that the curves collapse well at early times less than 0.1 nondimensional time units, and there is a more spread in the results at later times. These later times correspond to when the deformation of the plate panel has started to grow. A clear pattern with the D_{22} values of the panel is not easily seen except that some impact velocities for the $D_{22} = 205$ Pa m^3 panel seem to have a lower slope than the rest of the curves.

The spray root velocity time history, shown in Fig. 18, was computed by taking the time derivative of the spray root time history from the experimental program. It is seen that the velocities

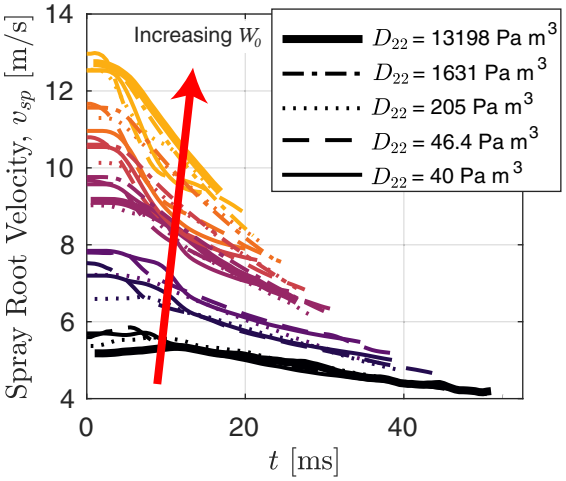

FIG. 18. Summary of spray root velocity for all panels in experimental program at all impact velocities. The color gradient becomes lighter as the impact velocity increases.

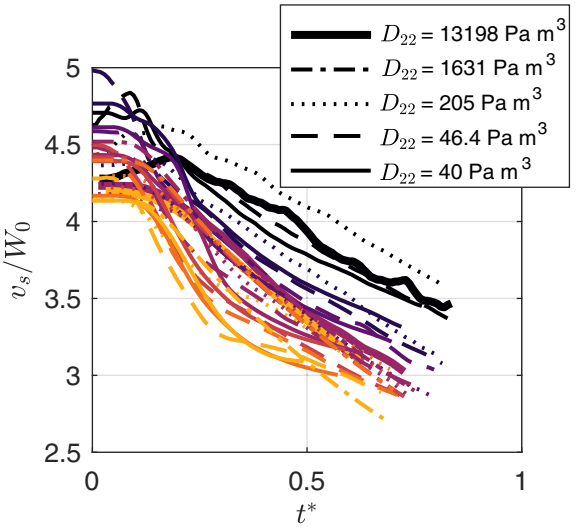

FIG. 19. Summary of nondimensional spray root velocities in the experimental program. Velocity is normalized by the impact velocity, W_0, and the time is normalized by the wetting time. The color gradient becomes lighter as the impact velocity increases.

of the spray root start around the same values for each impact velocity case, i.e., like colors are clustered together. The instantaneous velocities decrease faster in time for the cases with higher W_0. Discernible patterns with D_{22} are not easily seen. The spray root velocity is nondimensionalized in Fig. 19. The velocity is normalized by the impact velocity, and the time is again normalized by the wetting time. The timescales show better agreement than the dimensional plot. While the band of the spread is not very large—it only spans 1 dimensionless velocity unit in the vertical direction—there is a pattern in that the conditions with a higher W_0 have lower nondimensional velocities than the cases with lower W_0. This could be due to the fact that the rigid body velocity of the wedge is decreasing faster for the higher impact velocity conditions; see Fig. 7(b). The instantaneous velocities decrease faster due to the buoyancy and added mass effects when the impact velocity is higher.

Figure 20 displays numerical predictions of the spray root position along the centerline of the panel over time for the flexible aluminum wedge. While the general trends are similar, it is worth noting that the simulation consistently shows the spray root lagging behind the experimental results, regardless of the impact velocity. Section II B discussed the modeling assumptions, which consider the panel as a rigid surface from the hydrodynamic model's perspective. The results shown in Fig. 20 are counterintuitive because one would anticipate the spray root to propagate faster along a rigid surface compared to a deforming surface, as demonstrated by the experimental observations depicted in Fig. 16. Furthermore, comparison of the numerical and experimental spray root velocity time histories, shown in Fig. 21, indicates that the spray root velocities predicted by the simulation are of equal or higher magnitude than those in the experiment. Since the wedge kinematics between the simulation and experiment agree quite well, it is likely that these inconsistencies may be attributed to the different techniques used in the simulation and experiment to locate the spray root and compute its instantaneous velocity.

Higher loads are associated with higher impact velocities and therefore higher panel deformations. Higher deformations result in a longer time for the pressure wave and spray root to travel along the bottom of the plate panel. In Fig. 22, the time (horizontal axis) for the peak pressure to reach each sensor location (vertical axis) is plotted for the experimental runs. There are discrete points corresponding to each pressure sensor location. The slopes of these curves, i.e., the velocity of the

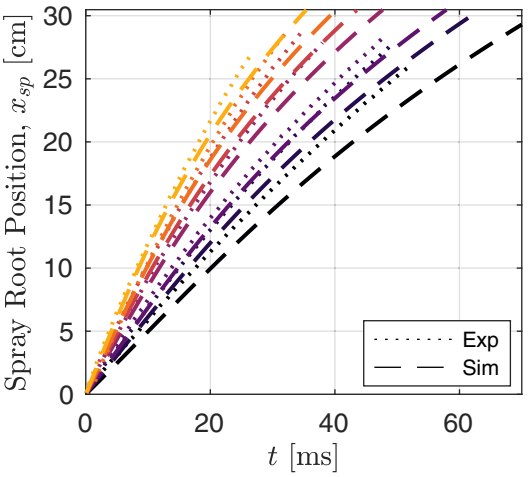

FIG. 20. Summary of spray root position time histories for the flexible aluminum panel for the experiment and simulation at all impact velocities. The color gradient becomes lighter as the impact velocity increases.

pressure wave, is steepest when D_{22} is highest and less steep as D_{22} decreases (corresponding to the symbol types). The color gradient becomes lighter as the impact velocity increases and the slope of the pressure wave position versus time becomes more steep, or faster, with increasing impact velocity. These behaviors intuitively make sense.

Figure 23 presents the observations from Fig. 22 in nondimensional form. The positions of each pressure sensor are normalized by the plate length, while the time for the peak pressure to reach each sensor location is normalized by the wetting time. The curve seems to collapse well for the first pressure sensor location, but deviations are seen as the pressure wave travels along the length of the bottom of the wedge. This corresponds to the deformation in the plate causing the path the pressure wave must travel to increase by a small amount. The nondimensional parameters used here do not account for flexural rigidity or deformation of the panel.

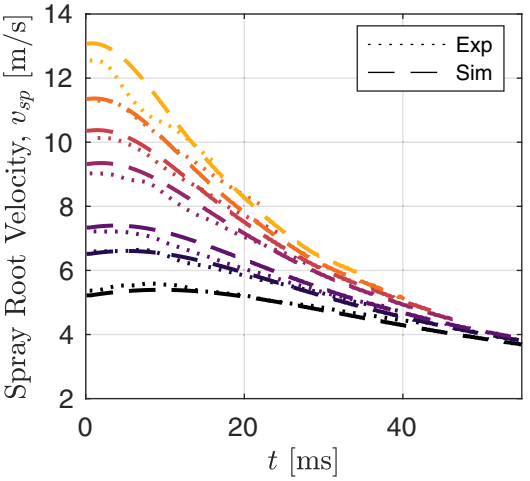

FIG. 21. Summary of spray root velocity for flexible aluminum panels for the experiment and simulation at all impact velocities. The color gradient becomes lighter as the impact velocity increases.

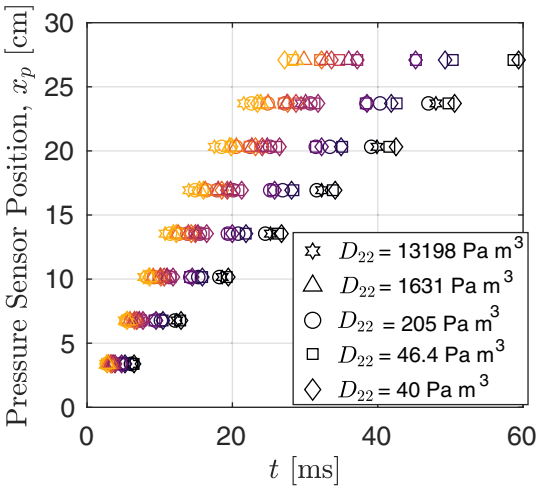

FIG. 22. Time of pressure peak arrival (horizontal axis) at each pressure sensor location (vertical axis). The color gradient becomes lighter as the impact velocity increases.

Figure 24 depicts the same information as Fig. 22; however, a subset of the experimental data is shown, for flexible aluminum only, and shows a comparison to the numerical model. The inset shows how well the time of arrival compares between the numerical prediction and the measured experiment. A clearer interpretation of the data can be seen in Fig. 25, in which the time of arrival and pressure sensor locations have been nondimensionalized by wetting time and plate length, respectively. In this figure, which is nearly identical to Fig. 23, the simulation results for the flexible aluminum panel collapse reasonably well, while the experimental data exhibit more spread relative to the numerical model. This is consistent with previous results shown in Fig. 23, which indicate greater spread in time of arrival for flexible aluminum when compared with the other panel materials. While the cause of this discrepancy is not known at this time, it speaks to the value of a combined experimental and computational study, and it will be explored further in future work.

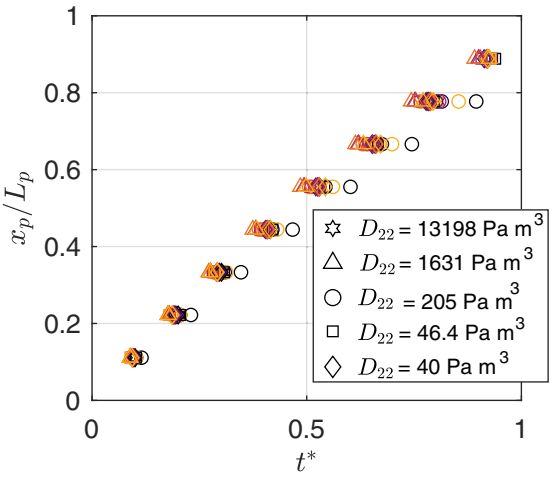

FIG. 23. Nondimensional time of pressure peak arrival (horizontal axis) at each nondimensional pressure sensor location (vertical axis). The position of the pressure sensor is normalized by the plate length, and the time is normalized by the wetting time. The color gradient becomes lighter as the impact velocity increases.

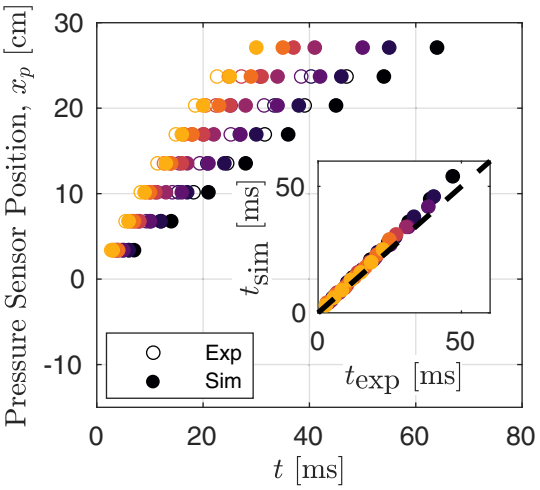

FIG. 24. Comparison of the experimental and numerical time of pressure peak arrival (horizontal axis) at each pressure sensor location (vertical axis) for flexible aluminum panel. The color gradient becomes lighter as the impact velocity increases. The inset shows the correlation between time of arrival between the simulation prediction and experimental measurement.

It was seen in the experimental study that the nondimensional pressure wave behavior exhibits more spread than the corresponding results for the numerical study. The nondimensional time to reach each pressure sensor location was then plotted versus the hydroelasticity factor, R, to understand any dependencies on the structural flexural rigidity value. This plot is shown in Fig. 26 for the experiments only. The R value of 2 is shown as the cutoff between rigid and flexible behavior. In the rigid region, the times to reach each pressure sensor location are approximately constant. For ease of viewing, dotted black horizontal lines are plotted to show an average T^* value that

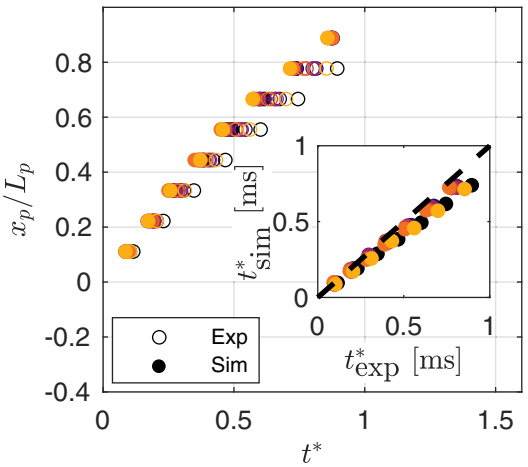

FIG. 25. Comparison of the experimental and numerical nondimensional time of pressure peak arrival (horizontal axis) at each nondimensional pressure sensor location (vertical axis) for flexible aluminum panels. The color gradient becomes lighter as the impact velocity increases. The position of the pressure sensor is normalized by the plate length, and the time is normalized by the wetting time. The inset shows the correlation between time of arrival between the simulation prediction and experimental measurement.

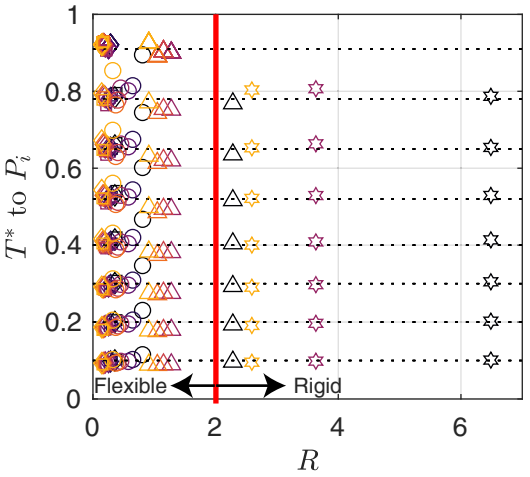

FIG. 26. The nondimensional time to reach each pressure sensor location vs the hydroelasticity factor, R. The color gradient becomes lighter as the impact velocity increases.

corresponds to the pressure wave reaching each sensor. At lower values of R, it is harder to see the behavior. So this plot is replotted in Fig. 27 for the flexible cases only. While there is some spread, especially at later T^* values, the nondimensional time of arrival at each sensor location is approximately constant relative to R.

Finally, the maximum deflection achieved at all times during the wetted period and all locations along the midspan curve is plotted versus R for all experimental conditions in Fig. 28. One maximum deflection value is chosen for each condition in the experimental program to compare versus R. Because deflection was not reported for the rigid condition (though it was verified to be approximately zero), the R values shown in the plot are not greater than 2. The behavior of the scatter plot shows that there is an exponential decay for the panels.

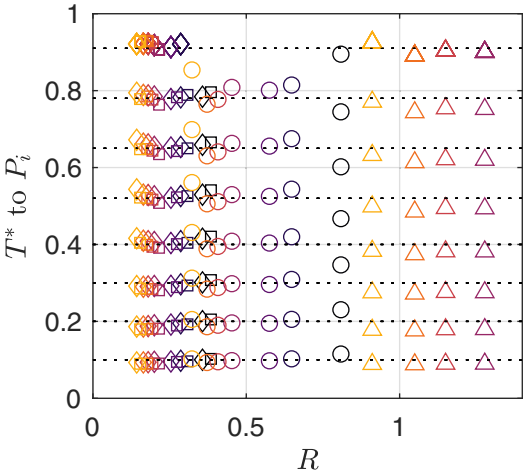

FIG. 27. The nondimensional time to reach each pressure sensor vs the hydroelasticity factor, R, for $R < 2$. The color gradient becomes lighter as the impact velocity increases.

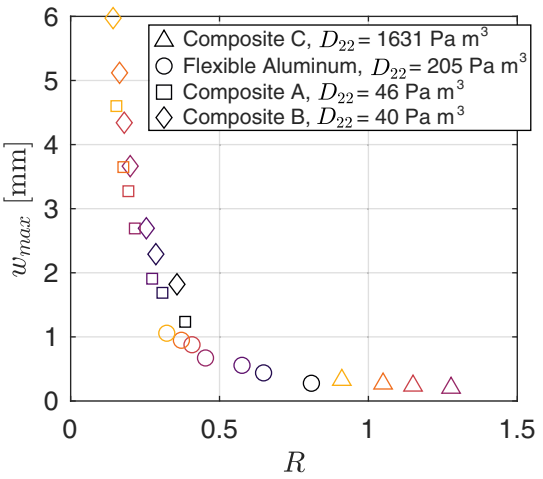

FIG. 28. Maximum deflection achieved during the wetted period vs hydroelasticity factor, R. The color gradient becomes lighter as the impact velocity increases.

V. CONCLUSIONS AND FUTURE DIRECTIONS

This paper focused on experimental measurements and simulations for the slamming of small craft using wedge water entry. The experimental setup involved measuring dynamic surface pressures on the bottom of the wedge, taking into account structural deflection, water contact line, and rigid body motions of the vertically constrained wedge.

The numerical model utilized a one-way coupled nonlinear hydrodynamic code, combined with an Euler-Bernoulli beam finite element solver, to simulate the water entry process. The model considered five different conditions of panel flexural rigidity, leading to varying deformations on the bottom panel and resulting in different fluid characteristics.

The spray root time histories were analyzed for various panel cases and impact velocities, revealing intriguing patterns. As the impact velocity increased, the spray root curves exhibited greater spread, with higher panel deformations corresponding to higher velocities. Additionally, the stiffness of the panel, determined by the flexural rigidity parameter D_{22}, influenced the spray root position and velocity. The experimental results, when nondimensionalized, demonstrated consistent trends, even though the panel flexural rigidity values varied significantly.

The spray root velocity time history analysis provided further insights into the impact velocity and rigid body motion effects. Early-time spray root velocities were seen to cluster together at similar impact speeds regardless of panel type, and the instantaneous velocities decreased more rapidly over time for higher impact speeds. Nondimensionalization of the spray root velocity highlighted better agreement among the timescales, revealing that conditions with higher impact velocities yielded lower nondimensional velocities due to the faster decrease in rigid body velocity caused by buoyancy and added mass effects.

Comparisons were also made between the experimental results and numerical predictions for the spray root position and velocity. Notably, the numerical simulation consistently showed the spray root lagging behind the experimental observations. Despite anticipating faster propagation along a rigid surface, as expected from the hydrodynamic model's perspective, the experimental data demonstrated that the deforming surface led to a faster spray root progression. The hydrodynamic model solves for the spray root velocity directly and integrates the solution in time to compute a spray root location, while the spray root velocity is derived from direct measurements of spray root location in the experiment. These different approaches likely account for the discrepancies observed between simulation and experiment.

The investigation of the pressure wave behavior along the bottom of the plate panel provided valuable insights into the effects of panel deformations. The time for the peak pressure to reach each sensor location exhibited steeper slopes for higher flexural rigidity values, indicating faster pressure wave propagation. Nondimensionalization of the pressure wave position versus time plot demonstrated good agreement for the first sensor location, but deviations were observed as the pressure wave traveled along the length of the wedge bottom due to plate deformations altering the wave's path.

Furthermore, the nondimensional time to reach each pressure sensor location was analyzed with respect to the hydroelasticity factor, revealing interesting dependencies. In the rigid region, the times to reach the peak pressure at each sensor remained approximately constant, regardless of the flexural rigidity value. The analysis of maximum deflection against the hydroelasticity factor showcased an exponential decay trend for the panels.

In summary, the experimental study provided crucial insights into the dynamics of wedge water entry, shedding light on the influence of impact velocities, panel deformations, and flexural rigidity. The observed patterns and behaviors deepen our understanding of slamming phenomena, facilitating the design and analysis of various high-speed craft, seaplane landings, and biological flows involving water entry. The experimental results serve as a valuable benchmark for future investigations and can guide the development and refinement of numerical models and simulation techniques in this field.

ACKNOWLEDGMENTS

We wish to acknowledge the support of the Office of Naval Research (Grants No. N00014-16-1-3188 and No. N00014-20-1-2254). We would also like to thank Dr. Carolyn Judge for allowing us to adapt her hydrodynamic code. The authors also acknowledge the other students who have contributed to the experimental program, particularly Dr. Zhongshu Ren, Jason Provost, Lauren Honey, and Matthew Brown.

[1] T. von Karman, The impact of seaplane floats during landing, in *National Advisory Committee on Aeronautics*, Technical Note 321, Washington, D.C. (1929).
[2] H. Wagner, *The Landing of Seaplanes*, Technical Report Technical Note 622, 254, NACA (1932).
[3] S. Abrate, Hull slamming, Appl. Mech. Rev. **64**, 060803 (2011).
[4] O. M. Faltinsen, Hydroelastic slamming, J. Mar. Sci. Technol. **5**, 49 (2000).
[5] L. Vincent, T. Xiao, D. Yohann, S. Jung, and E. Kanso, Dynamics of water entry, J. Fluid Mech. **846**, 508 (2018).
[6] E. Gregorio, E. Balaras, and M. C. Leftwich, How olympic divers manipulate the air cavity to reduce splash, Bull. Am. Phys. Soc. A01.00007 (2022).
[7] A. Pandey, J. Yuk, B. Chang, F. E. Fish, and S. Jung, Slamming dynamics of diving and its implications for diving-related injuries, Sci. Adv. **8**, eabo5888 (2022).
[8] A. R. J. M. Lloyd, *Seakeeping: Ship Behaviour in Rough Weather* (Horwood, Gosport, UK, 1989).
[9] O. Faltinsen, *Hydrodynamics of High-speed Marine Vehicles* (Cambridge University Press, New York, 2005).
[10] E. Zarnick, A nonlinear mathematical model of motions of planing boat in regular waves, Tech. Rep. DTNSRDC-78/032 (David W. Taylor Naval Ship R&D Center, Carderock, MD, 1978).
[11] M. J. Javaherian, R. Royce, R. Datla, and C. M. Gilbert, Hydrodynamics of high-speed planing craft: Savitsky method and 2d+ t approach, in *SNAME International Conference on Fast Sea Transportation* (OnePetro, Providence, 2021).
[12] W. Vorus, A flat cylinder theory for vessel impact and steady planing resistance, J. Ship Res. **40**, 89 (1996).

[13] C. Judge, A. Troesch, and M. Perlin, Initial water impact of a wedge at vertical and oblique angles, J. Eng. Math. **48**, 279 (2004).
[14] J. L. Armand and R. Cointe, Hydrodynamic impact analysis of a cylinder, in *International Offshore Mechanics and Arctic Engineering, Symposium 5* (ASME, Tokyo, Japan, 1986).
[15] R. Cointe and J.-L. Armand, Hydrodynamic impact analysis of a cylinder, J. Offshore Mech. Arctic Eng. **109**, 237 (1987).
[16] S. Howison, J. Ockendon, and S. Wilson, Incompressible water-entry problems at small deadrise angles, J. Fluid Mech. **222**, 215 (1991).
[17] R. Zhao and O. Faltinsen, Water entry of two-dimensional bodies, J. Fluid Mech. **246**, 593 (1993).
[18] C. Q. Judge, A theory for asymmetric vessel impact with horizontal impact velocity, Ph.D. thesis, The University of Michigan (2000).
[19] L. Xu, A theory for asymmetrical vessel impact and steady planing, Ph.D. thesis, The University of Michigan (1998).
[20] R. L. Bisplinghoff and C. S. Doherty, Some studies of the impact of vee wedges on a water surface, J. Franklin Inst. **253**, 547 (1952).
[21] S. Chuang, Slamming of rigid wedge-shaped bodies with various deadrise angles, Tech. Rep. 2268 (David Taylor Model Basin, Carderock, MD, 1966).
[22] E. Yettou, A. Desrochers, and Y. Champoux, Experimental study on the water impact of a symmetrical wedge, Fluid Dyn. Res. **38**, 47 (2006).
[23] T. Tveitnes, A. Fairlie-Clarke, and K. Varyani, An experimental investigation into the constant velocity water entry of wedge-shaped sections, Ocean Eng. **35**, 1463 (2008).
[24] S. Lewis, D. Hudson, A. Turnock, and D. J. Taunton, Impact of a free-falling wedge with water: Synchronized visualization, pressure and acceleration measurements, Fluid Dyn. Res. **42**, 035509 (2010).
[25] C. M. Ikeda and C. Q. Judge, Slamming pressures on the bottom of a free-falling vertical wedge, in *APS Meeting Abstracts* (APS Division of Fluid Dynamics, Pittsburgh, 2013), p. G28.004.
[26] C. Ikeda and C. Judge, Pressure stagnation line on a planing hull in calm water (APS Division of Fluid Dynamics Meeting Abstracts, San Francisco, USA, 2014).
[27] Z. N. Dobrovol'skaya, On some problems of similarity flow of fluid with a free surface, J. Fluid Mech. **36**, 805 (1969).
[28] A. A. Korobkin and Y. M. Scolan, Three-dimensional theory of water impact. Part 2. Linearized wagner problem, J. Fluid Mech. **549**, 343 (2006).
[29] S. M. Mousaviraad, Z. Wang, and F. Stern, Urans studies of hydrodynamic performance and slamming loads on high-speed planing hulls in calm water and waves for deep and shallow conditions, Appl. Ocean Res. **51**, 222 (2015).
[30] O. M. Faltinsen, Water entry of a wedge by hydroelastic orthotropic plate theory, J. Ship Res. **43**, 180 (1999).
[31] G. K. Kapsenberg, Slamming of ships: Where are we now?, Philos. Trans. **369**, 2892 (2011).
[32] C. Ikeda, J. Wilkerling, and J. Duncan, The implosion of cylindrical shell structures in a high-pressure water environment, Proc. R. Soc. A **469**, 20130443 (2013).
[33] Z. Qin and R. Batra, Local slamming impact of sandwich composite hulls, Int. J. Solids Struct. **46**, 2011 (2009).
[34] D. J. Piro and K. J. Maki, Hydroelastic analysis of bodies that enter and exit water, J. Fluids Struct. **37**, 134 (2013).
[35] R. Panciroli, S. Abrate, and G. Minak, Dynamic response of flexible wedges entering the water, Compos. Struct. **99**, 163 (2013).
[36] R. Panciroli, Water entry of flexible wedges: Some issues on the fsi phenomena, Appl. Ocean Res. **39**, 72 (2013).
[37] R. Panciroli and M. Porfiri, Analysis of hydroelastic slamming through particle image velocimetry, J. Sound Vib. **347**, 63 (2015).
[38] J. Mesa and K. Maki, Numerical hydroelastic analysis of slamming for high speed vessels, in *Proceedings of the 14th International Conference on Fast Sea Transportation* (SNAME, Nantes, France, 2017).

[39] A. Shams and M. Porfiri, Treatment of hydroelastic impact of flexible wedges, J. Fluids Struct. **57**, 229 (2015).
[40] C. Ikeda and B. Taravella, Analytical predictions of the structural response of high-speed planing craft, in *SNAME Maritime Convention* (SNAME, Bellevue, 2016).
[41] R. D. Fisher, J. N. Gilbert, and C. M. Gilbert, A semi-theoretical method of estimating pressure & structural response on a flexible wedge, in *SNAME Maritime Convention* (OnePetro, Tacoma, 2019).
[42] Z. Ren, M. J. Javaherian, and C. M. Gilbert, A verification and validation study on a loosely two-way coupled hydroelastic model of wedge water entry, J. Ship Res. **2023**, 1 (2023).
[43] Z. Ren and C. M. Ikeda, On the hydro-elastic response of a flexible wedge to vertical slamming, Naval Eng. J. **129**, 51 (2017).
[44] Z. Ren, M. J. Javaherian, Z. Wang, C. Judge, F. Stern, and C. Ikeda-Gilbert, Structural response due to the hydroelasticity of a slamming impact of a small craft in waves, in *Proceedings of the 32nd Symposium on Naval Hydrodynamics* (Office of Naval Research, Hamburg, Germany, 2018).
[45] Z. Ren, W. Zhaoyuan, F. Stern, C. Judge, and C. Ikeda-Gilbert, Vertical water entry of a flexible wedge into calm water: A fluid-structure interaction experiment, J. Ship Res. **63**, 41 (2019).
[46] Z. Ren, M. J. Javaherian, and C. M. Gilbert, Kinematic and inertial hydroelastic effects caused by vertical slamming of a flexible v-shaped wedge, J. Fluids Struct. **103**, 103257 (2021).
[47] Z. Ren, M. J. Javaherian, and C. Gilbert, Vertical wedge drop experiments as a model for slamming, J. Ship Res. **66**, 297 (2022).
[48] M. Javaherian, Z. Ren, C. Judge, and C. Gilbert, Structural response due to the slamming of high-speed craft by water entry and towing tank experiments, in *Proceedings of the 33rd Symposium on Naval Hydrodynamics* (Office of Naval Research, Osaka, Japan, 2020).
[49] M. J. Javaherian, Z. Ren, and C. M. Gilbert, Flow visualization, hydrodynamics, and structural response of a flexible wedge in water entry experiments, J. Ship Res. **67**, 59 (2023).
[50] A. Bhardwaj, M. J. Javaherian, and N. Husser, Vertical wedge water-entry through experiments and simulation to explore three-dimensional hydrodynamic flow characteristic, in *SNAME International Conference on Fast Sea Transportation* (OnePetro, Providence, 2021).